

Effect of impact velocity on spall behaviors of nanocrystalline iron: Molecular dynamics study

Li-Qiong Chen(陈利琼), Kui Zhao(赵奎), Kai Zhang(张开), Ze-Zhi Wen(文泽智), Hou-Jin Mei(梅后金), and Zhen-Bao Xiong(熊珍宝)

Citatio: Chin. Phys. B, 2025, 34 (**9**): 096201. DOI: 10.1088/1674-1056/add4ff
http://cpb.iphy.ac.cn; http://iopscience.iop.org/cpb

What follows is a list of articles you may be interested in

Elastic-plastic behavior of nickel-based single crystal superalloys with *γ*-*γ*′ phases based on molecular dynamics simulations

Jing-Zhao Cao(曹景昭), Yun-Guang Zhang(张云光), Zhong-Kui Zhang(张中奎), Jiang-Peng Fan(范江鹏), Qi Dong(董琪), and Ying-Ying Fang(方盈盈)

Chin. Phys. B, 2025, 34 (**4**): 046204. DOI: 10.1088/1674-1056/adb40f

Novel high-temperature-resistant material $SbLaO_3$ with superior hardness under high pressure

Haoqi Chen(陈浩琦), Haowen Jiang(姜皓文), Xuehui Jiang(姜雪辉), Jialin Wang(王佳琳), Chengyao Zhang(张铖瑶), Defang Duan(段德芳), Jing Dong(董晶), and Yanbin Ma(马艳斌)

Chin. Phys. B, 2025, 34 (**2**): 026201. DOI: 10.1088/1674-1056/ad989e

Influence of temperature, stress, and grain size on behavior of nano-polycrystalline niobium

Yu-Ping Yan(晏玉平), Liu-Ting Zhang(张柳亭), Li-Pan Zhang(张丽攀), Gang Lu(芦刚), and Zhi-Xin Tu(涂志新)

Chin. Phys. B, 2024, 33 (**7**): 076201. DOI: 10.1088/1674-1056/ad3b83

High-pressure elastic anisotropy and superconductivity of hafnium: A first-principles calculation

Cheng-Bin Zhang(张成斌), Wei-Dong Li(李卫东), Ping Zhang(张平), and Bao-Tian Wang(王保田)

Chin. Phys. B, 2021, 30 (**5**): 056202. DOI: 10.1088/1674-1056/abd6f6

Shock-induced migration of asymmetry tilt grain boundary in iron bicrystal: A case study of Σ3 [110]

Xueyang Zhang(张学阳), Kun Wang(王昆), Jun Chen(陈军), Wangyu Hu(胡望宇), Wenjun Zhu(祝文军), Shifang Xiao(肖时芳), Huiqiu Deng(邓辉球), Mengqiu Cai(蔡孟秋)

Chin. Phys. B, 2019, 28 (**12**): 126201. DOI: 10.1088/1674-1056/ab4f61

Effect of impact velocity on spall behaviors of nanocrystalline iron: Molecular dynamics study

Li-Qiong Chen(陈利琼), Kui Zhao(赵奎), Kai Zhang(张开)[†],
Ze-Zhi Wen(文泽智), Hou-Jin Mei(梅后金), and Zhen-Bao Xiong(熊珍宝)

School of Petroleum Engineering, Southwest Petroleum University, Chengdu 610000, *China*

(Received 1 March 2025; revised manuscript received 28 April 2025; accepted manuscript online 7 May 2025)

This study investigates the effect of shock velocity (u_p) on damage evolution mechanisms in nanocrystalline iron via molecular dynamics simulations. As u_p increases, shock wave propagation accelerates, and stress distribution transitions from grain boundary concentration to homogeneity. This causes a transition in fracture mode from cleavage to ductile behavior. When u_p exceeds 1.5 km·s^{-1}, micro-spallation emerges as the dominant failure mode. During micro-spallation, localized melting within the material impedes the propagation of the shock wave. As u_p increases, the growth rate of the void volume fraction initially rises but then decreases. Higher u_p leads to earlier void nucleation. At lower u_p, the cavitation of the model is mainly characterized by the growth and penetration of a few voids. With increasing u_p, the number of voids grows, and their interactions expand the delamination damage region. The spall strength demonstrates stage-specific dependence on u_p. In the classical spallation stage (C_I), temperature softening reduces spall strength. In the plastic strengthening regime (C_II), strain hardening enhances spall strength. In the micro-spallation stage (M_III), further increases in u_p cause melting during tensile and compressive phases, reducing spall strength. Finally, in the compression-melting regime (M_IV), local temperatures exceed the melting point, diminishing plastic damage and accelerating spall strength reduction. This study provides new insights into the dynamic response of nanocrystalline iron.

Keywords: nanocrystalline iron, shock response, fragmentation, spallation, molecular dynamics

PACS: 62.50.Ef, 02.70.Ns, 81.40.Np

DOI: 10.1088/1674-1056/add4ff **CSTR:** 32038.14.CPB.add4ff

1. Introduction

Iron, one of the most abundant metals on the Earth, has long been recognized as a crucial structural material due to its exceptional mechanical properties, such as high strength, hardness, and toughness.[1–3] These attributes have led to its widespread application across various engineering disciplines, including construction, machinery, and aerospace. However, with the continuous advancement of science and technology, iron-based materials are increasingly subjected to more demanding operating conditions that require them to endure extreme factors, including elevated temperatures, high pressures, and high strain rates.[4–6] Furthermore, since these materials inevitably experience impact loading during service, their performance is significantly compromised under such conditions, making them susceptible to damage mechanisms such as phase transitions, spallation, and complex fragmentation.[7–10] Therefore, it is crucial to conduct in-depth studies on the damage evolution and dynamic response mechanisms of iron-based materials under impact loading to better understand and mitigate these risks.

Spallation induced by shock waves propagating in two opposite directions is one of the most common forms of dynamic material damage under shock loading. The spalling process is often accompanied by phenomena such as shock-induced phase transitions, shock plasticity, and dynamic fragmentation. With the development of various dynamic high-pressure loading methods and measurement techniques, scholars have experimentally observed these phenomena under shock loading conditions.[11–14] In 1956, Bancroft *et al*. conducted dynamite impact experiments that revealed iron undergoes a phase transition at 13-GPa impact strength, which marked the beginning of phase transition studies under impact loading.[15] Furthermore, Shockey *et al*. found that the spall behavior of steel subjected to high-velocity impacts is influenced by phase transition.[16] Later, Yaakobi *et al*. confirmed the transformation of α-Fe to ε-Fe under shock loading conditions using x-ray absorption fine structure spectroscopy (XRAFS) and femtosecond laser loading techniques (FELT), both of which are advanced techniques for examining atomic-level structural changes under high-pressure environments.[17,18] Additionally, Wang *et al*. summarized possible phase transition mechanisms for the transformation of body-centered cubic (BCC) to hexagonal close-packed (HCP) in iron by measuring the lattice constants at different pressures.[19]

Experimental methods face intrinsic challenges in studying microscopic structural evolution, stemming from scale limitations.[20–23] With the advancement of computer technol-

[†]Corresponding author. E-mail: 202221000831@stu.swpu.edu.cn

© 2025 Chinese Physical Society and IOP Publishing Ltd. All rights, including for text and data mining, AI training, and similar technologies, are reserved.

ogy, molecular dynamics has emerged as a powerful cross-scale simulation technique, widely employed in the study of deformation and damage mechanisms in iron-based materials. In 2002, Kadau *et al.* were the first to observe the structural transition from BCC to HCP in iron under shock compression using classical molecular dynamics simulations.[13] Subsequently, Gunkelmann *et al*. enhanced the interatomic potential for iron, which enabled a more accurate representation of its phase transition and plastic behavior. Their study demonstrated that the shock wave structure evolves with increasing shock intensity, transitioning from elastic–plastic behavior to an elastic–plastic-phase transition, outlining the plastic deformation mechanism, including the formation of dislocation loops, their interaction with grain boundaries, and the subsequent creation of spiro-dislocations.[24,25] Additionally, Wang *et al*. developed a new modified analytical embedded atom model (MAEAM) potential. Their work indicated that nanocrystalline iron undergoes two distinct modes of phase transition coupling under impact loading and proposed two phase transition mechanisms: stress-assisted and strain-induced phase transition mechanisms.[26,27] Moreover, molecular dynamics simulations have revealed phenomena such as deformation twinning and hole nucleation during phase transitions, which correspond with experimental observations.[28,29]

Phase transitions and plasticity under impact loading tend to nucleate near defects, prompting researchers to investigate the influence of initial internal structures and surface/interface defects of iron-based materials on microstructural evolution. Sheng *et al*. investigated the effect of vacancy concentration on plasticity and phase transition processes in single-crystal iron. They found the vacancy and vacancy-induced dislocation loops promoted the nucleation and growth of phase transitions.[30] Furthermore, Huang *et al*. analyzed the shock response behavior of single-crystal iron containing edge-type dislocations and observed a shift in the active dislocation slip mechanism from $\{110\}\langle 111\rangle$ to $\{112\}\langle 111\rangle$.[31] Zhang *et al*. investigated the effects of grain boundaries on two mechanisms of phase deformation nucleation, revealing that asymmetric grain boundaries are more susceptible to migration under impact loading.[32,33] Wu *et al*. investigated the impact orientation effect of single-crystal iron containing cylindrical holes and found that dislocation rings appeared near the holes when impacted along the [110] and [111] grain directions, while no dislocations were observed when impacted along the [001] grain direction.[34] Additionally, Li *et al*. found that both stress-assisted and strain-induced phase transition mechanisms occurred during hole collapse.[35] Concurrent studies have demonstrated that the presence of holes significantly reduces the pressure threshold for phase transition, thereby facilitating the generation of new phases and promoting their formation.[36]

Significant progress has been made in the field of impact response of iron-based materials. However, most current studies primarily focus on elucidating the phase transformations and plasticity mechanisms of iron under spall damage conditions, with most investigations concentrating on single-crystal iron. Further investigations are required to fully understand the spall damage behavior of nanocrystalline iron under dynamic impact loading conditions. This study investigates the dynamic impact response of nanocrystalline iron over a wide range of impact velocities (u_{p}) using nonequilibrium molecular dynamics simulations (NEMD). The emphasis is on the effect of impact velocity (u_{p}) on spall damage evolution and spall strength. The structure of the paper is as follows: Section 2 details the methodologies used in atomic modeling, simulations, and analysis; Section 3 presents the results and discussion; and Section 4 concludes the study.

2. Methodologies

The open-source software, large-scale atomic/molecular parallel simulator (LAMMPS), was employed for the simulations in this study.[37] The interactions between iron atoms are modeled using the modified version of the Ackland potential, which has been demonstrated to accurately describe phase transitions and twinning mechanisms in iron crystal.[38,39] This potential has played a key role in advancing research, particularly in the understanding of high-pressure phase transition mechanisms and the governing principles of phase deformation.[24,29,40,41]

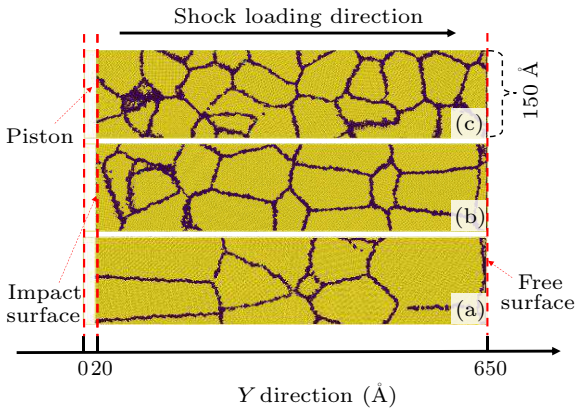


Fig. 1. Atomic computational model of nanocrystalline iron after equilibration: (a) model I, (b) model II, and (c) model III.

The initial atomistic systems have dimensions of 15 nm (X), 65 nm (Y), and 15 nm (Z). For comparative purposes, the Voronoi method was employed to partition the computational domain into 10, 20, and 30 Tyson polygonal grains. Subsequently, three isotropic polycrystalline iron models were generated by introducing randomly oriented BCC units into each grain, as illustrated in Fig. 1. Furthermore, a rigid piston, with a length of 20 Å, is placed at the left extremity of all models to generate impact loading. Seven simulations were con-

ducted, with velocities of $u_p = 0.5$, 0.75, 1.0, 1.5, 2.0, 2.5, and 3.0 km·s^{-1}, respectively.

The kinetic evolution of all the samples consisted of three stages: relaxation and shock and unloading, with a time step of 1 fs for each phase. In the relaxation stage, the energy minimization was initially accomplished through the implementation of the conjugate gradient (CG) method. Subsequently, the model underwent a reduction from 700 K to 10 K at 0 bar (1 bar = 10^5 Pa) via high-temperature annealing under the normal systematic synthesis (NVT) condition. This process was undertaken to eliminate the effects of noise and to establish a stable initial system. The impact stage is executed under the micro-regular system category (NVE). The X and Z boundaries are periodic, and the boundary along the loading orientation (Y) is kept free. The velocity of the "piston" is controlled to generate shock waves with different velocities in the y-direction, thereby realizing the shock loading. The loading duration is 10 ps. During the unloading stage, the piston velocity was terminated, and the model's damage and destruction behavior was monitored for a process of 20 ps.

The simulation results are visualized using the software OVITO.[42] Additionally, faceted element analysis is employed to examine the kinetic and thermodynamic properties of the model. This process involves slicing the model along the y-axis into smaller blocks and averaging physical quantities, such as atomic density, stress, and temperature, within each block. This systematic approach facilitates the investigation of the model's dynamic behavior and thermodynamic properties.

3. Results and discussion

3.1. Free surface velocity histories and damage process

Spallation is a characteristic form of damage that occurs under conditions of impact loading. The evolution of the free surface velocity (FSV) is a key indicator of the spall damage behavior. Temporal profiles of the FSV for each of the three models, under varying impact velocities (u_p), are shown in Figs. 2(a)–2(c). A direct correlation exists between the impact velocities of the piston and the time required for the shock wave to propagate to the free surface. As the impact velocity (u_p) increases, the time for the shock wave to reach the free surface decreases, the peak FSV increases, and the model reaches the Hugoniot elastic limit more rapidly. This trend can be attributed to the higher impact energy resulting from increased piston velocities. Notably, when the impact velocity (u_p) increases to 0.75 km·s^{-1}, the FSV exhibits a noticeable rebound after reaching its peak. This rebound occurs because as the impact velocity of the piston rises, the rate of fracture surface formation also increases. Consequently, the reflected waves from the free surface are more likely to induce compressive waves at the fracture surface. In the case of $u_p = 3.0$ km·s^{-1}, the magnitude of the FSV rebound diminishes, which is attributed to localized melting within the model, hindering shock wave propagation. Importantly, the trend in FSV variation with impact velocities remains consistent across all three models, suggesting that grain size has a negligible effect on the evolution of spall damage in nanocrystalline iron. This observation aligns with findings from spall damage studies on other metallic materials.[43]

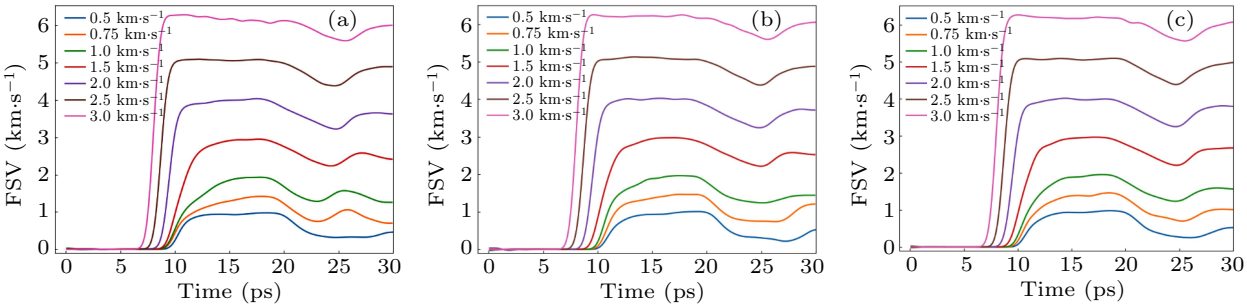


Fig. 2. Temporal profiles of free surface velocity at different shock velocities (u_p). (a) model I, (b) model II, (c) model III.

To investigate the damage process of the three models at different impact velocities, snapshots of the model evolution were extracted at time intervals of 10 ps, 15 ps, 20 ps, 25 ps, and 30 ps. Atomic stress in the Y-direction (pressure_yy) was used to color the atoms, where tensile stress is indicated by positive values and compressive stress by negative values. This approach enabled the visualization of stress distribution throughout the spallation evolution.

Based on the stress distributions presented in Figs. 3–5, it can be observed that as the impact velocity (u_p) increases, the compressive stress in the model increases gradually following the impact compression phase. During the relaxation and stretching phases, with impact velocities ranging from 0.5 km·s^{-1} to 1.0 km·s^{-1}, the tensile stress distribution exhibits a noticeable concentration along the grain boundaries, which becomes more pronounced at lower impact velocities. However, when the impact velocity exceeds 1.5 km·s^{-1}, the tensile stress shifts from a concentration along the grain boundaries to a more uniform and random distribution.

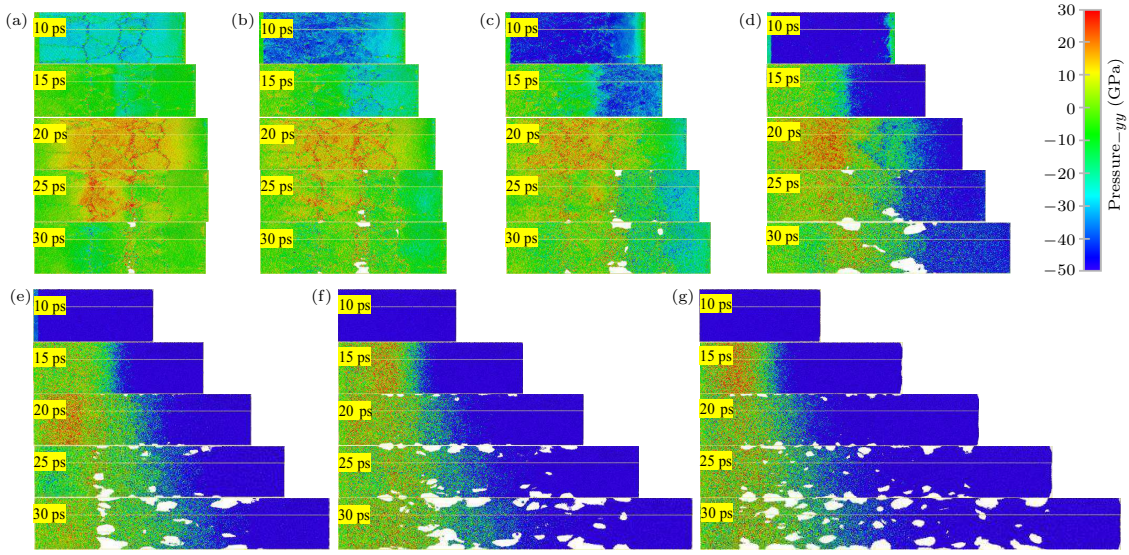


Fig. 3. Snapshots of shock-induced evolution of model I: (a) $u_{\mathrm{p}} = 0.5$ km·s^{-1}, (b) $u_{\mathrm{p}} = 0.75$ km· s^{-1}, (c) $u_{\mathrm{p}} = 1$ km·s^{-1}, (d) $u_{\mathrm{p}} = 1.5$ km·s^{-1}, (e) $u_{\mathrm{p}} = 2$ km·s^{-1}, (f) $u_{\mathrm{p}} = 2.5$ km·s^{-1}, (g) $u_{\mathrm{p}} = 3$ km·s^{-1}.

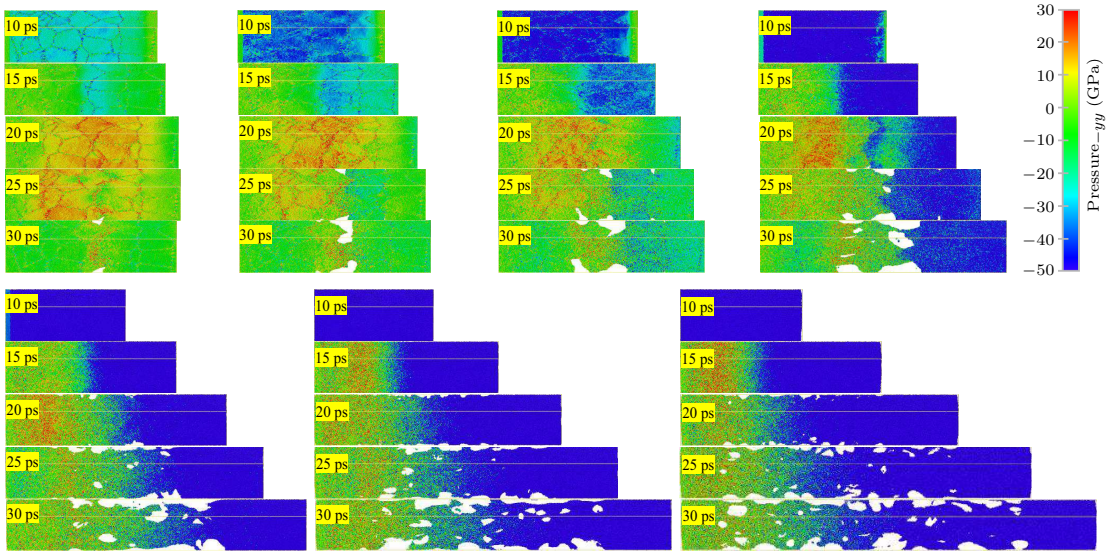


Fig. 4. Snapshots of shock-induced evolution of model II: (a) $u_{\mathrm{p}} = 0.5$ km·s^{-1}, (b) $u_{\mathrm{p}} = 0.75$ km· s^{-1}, (c) $u_{\mathrm{p}} = 1$ km·s^{-1}, (d) $u_{\mathrm{p}} = 1.5$ km·s^{-1}, (e) $u_{\mathrm{p}} = 2$ km·s^{-1}, (f) $u_{\mathrm{p}} = 2.5$ km·s^{-1}, (g) $u_{\mathrm{p}} = 3$ km· s^{-1}.

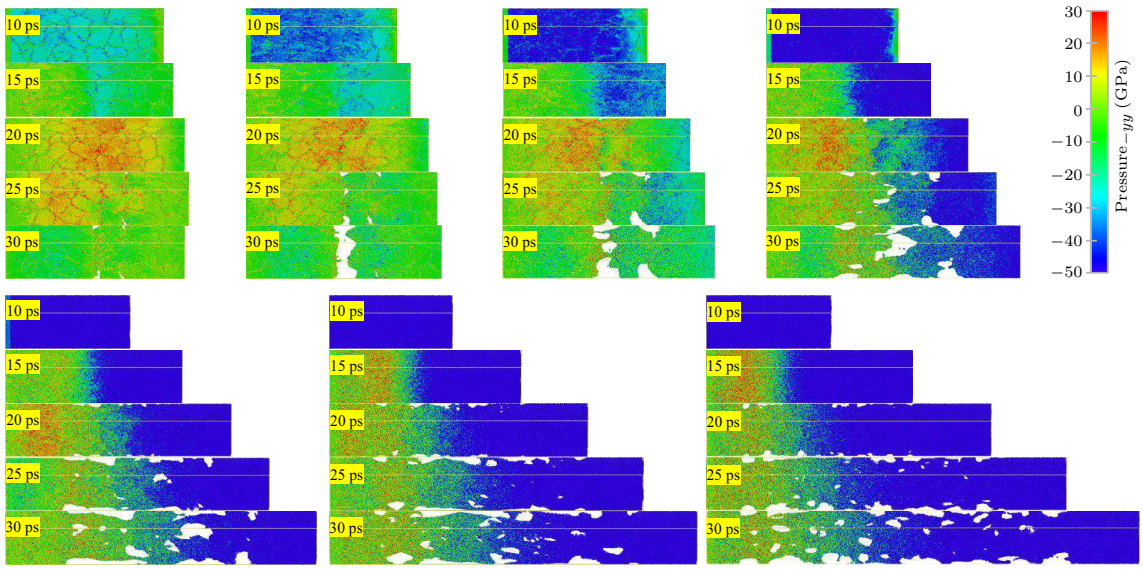


Fig. 5. Snapshots of shock-induced evolution of model III: (a) $u_{\mathrm{p}} = 0.5$ km·s^{-1}, (b) $u_{\mathrm{p}} = 0.75$ km· s^{-1}, (c) $u_{\mathrm{p}} = 1$ km·s^{-1}, (d) $u_{\mathrm{p}} = 1.5$ km·s^{-1}, (e) $u_{\mathrm{p}} = 2$ km·s^{-1}, (f) $u_{\mathrm{p}} = 2.5$ km·s^{-1}, (g) $u_{\mathrm{p}} = 3$ km· s^{-1}.

At lower impact velocities (u_p), spall fracture in polycrystals predominantly occurs along crystal boundaries. This phenomenon arises from the concentration of tensile stresses at grain boundaries during the relaxation and tensile phases of the impact event. This is because, at lower impact velocities (u_p), the models have not yet formed spall surfaces, leading to a rebound phenomenon at the free surface. As the impact velocity (u_p) exceeds 1.5 km·s^{-1}, the fracture mode of nanocrystalline iron transitions from along-crystal fracture to irregular fracture. Moreover, with further increases in impact velocity (u_p), melted crystals are observed to detach from the matrix during the spall process, as shown in panels (e) and (f) of Figs. 3–5. Additionally, A significant roughening of the free surface of the model is also observed. This change can be attributed to particle ejection triggered by the high-speed impact. Similar phenomena have been reported in studies of other metallic materials, indicating that metals may undergo micro-spall damage under high-velocity impact.[44]

3.2. Characteristics of cavitation under different shock velocities

The spallation mechanism is fundamentally governed by cavitation dynamics, which evolves through three distinct stages: (i) heterogeneous void nucleation, (ii) strain-rate dependent growth, and (iii) stress-driven coalescence. To establish the functional relationship between impact velocity (u_p) and void volume fraction, the constructed surface mesh (CSM) algorithm was employed, which incorporates the Voronoi tessellation for spatial discretization. A Gaussian-type probe with radius $r_p = 1.2a$ (~ 3.4 Å) enabled time-resolved characterization performed at $\Delta t = 1$ ps intervals, ensuring temporal resolution below the nucleation incubation period.

Figure 6 presents the statistical results of the void volume fraction for models with varying grain sizes at each time step. The results indicate that the variation trends of the void volume fraction are similar for models I–III at various impact velocities (u_p), suggesting that grain size has minimal influence on void growth behavior. However, all models demonstrate that the timing of hole nucleation is progressively advanced, and the growth rate of the void volume fraction accelerates with increasing u_p values. This indicates that the evolution of modeled micropores is highly sensitive to the impact velocity (u_p). Furthermore, In the case of $u_p = 0.5$ km·s^{-1}–1 km·s^{-1}, the void volume fraction displays a constant growth rate, exhibiting a discontinuous change. In contrast, under impact loading ranging from 1.5 km·s^{-1} to 3 km·s^{-1}, the growth rate of the void volume fraction initially increases and subsequently decreases. This suggests that the model experiences a distinct phase of void nucleation and growth during micro-spallation. Notably, the time interval for void nucleation is significantly reduced as the impact velocity (u_p) increases. For instance, in model I, the time for void nucleation to occur is approximately 14 ps–16 ps at an impact velocity (u_p) of 3 km·s^{-1}, whereas it is approximately 18 ps–21 ps at 1.5 km·s^{-1}.

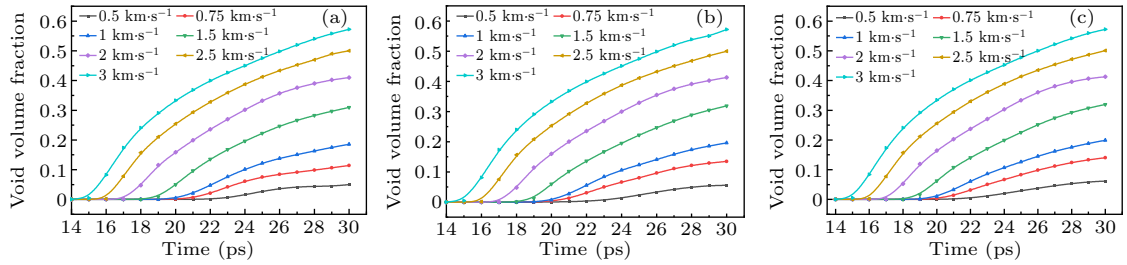


Fig. 6. Temporal profiles of void volume fraction at different impact velocities (u_p): (a) model I, (b) model II, (c) model III.

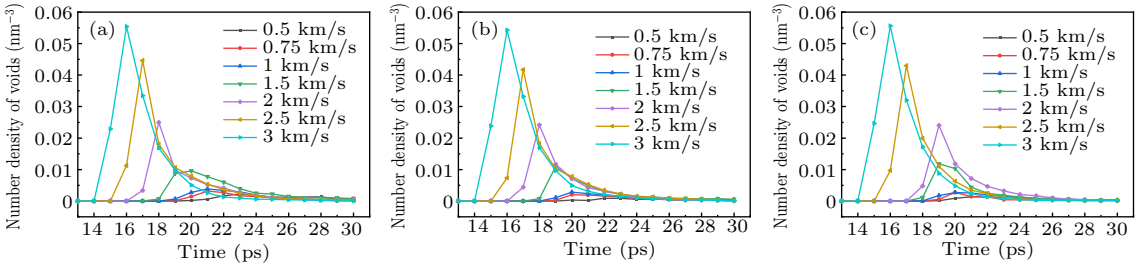


Fig. 7. Temporal profiles of the number density of voids at different impact velocities (u_p): (a) model I, (b) model II, (c) model III.

To investigate the interactions among voids during spallation and their evolutionary mechanisms, figure 7 illustrates the evolution of void number density in the three models under various shock loading conditions. As depicted in Fig. 7, the growth rate of the void number density during the nucleation stage increases with the impact velocity (u_p), while the nucleation time decreases as the impact velocity (u_p) increases, which is consistent with prior study.[46] Moreover, the peak value of the void number density exhibits a significant increase with increasing impact velocity (u_p), suggesting

that higher impact velocities (u_p) facilitate the nucleation of a greater number of voids. Notably, when the impact velocity (u_p) ranges from 0.5 km·s^{-1} to 1 km·s^{-1}, the void number density does not exhibit a sharp decline after reaching its peak value. However, when the impact velocity (u_p) exceeds 1.5 km·s^{-1}, the void number density initially undergoes a sharp decline and subsequently transitions into a phase of gradual reduction.

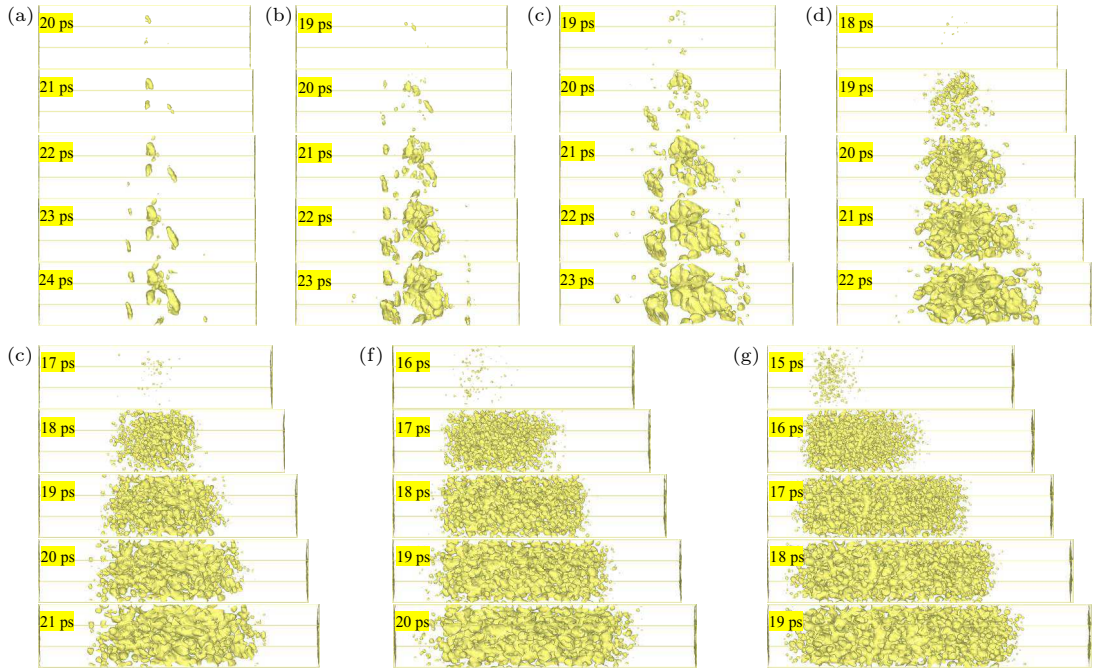


Fig. 8. Snapshots of shock-induced evolution of voids configurations for model II: (a) $u_p = 0.5$ km·s^{-1}, (b) $u_p = 0.75$ km·s^{-1}, (c) $u_p = 1$ km·s^{-1}, (d) $u_p = 1.5$ km·s^{-1}, (e) $u_p = 2$ km·s^{-1}, (f) $u_p = 2.5$ km·s^{-1}, (g) $u_p = 3$ km·s^{-1}.

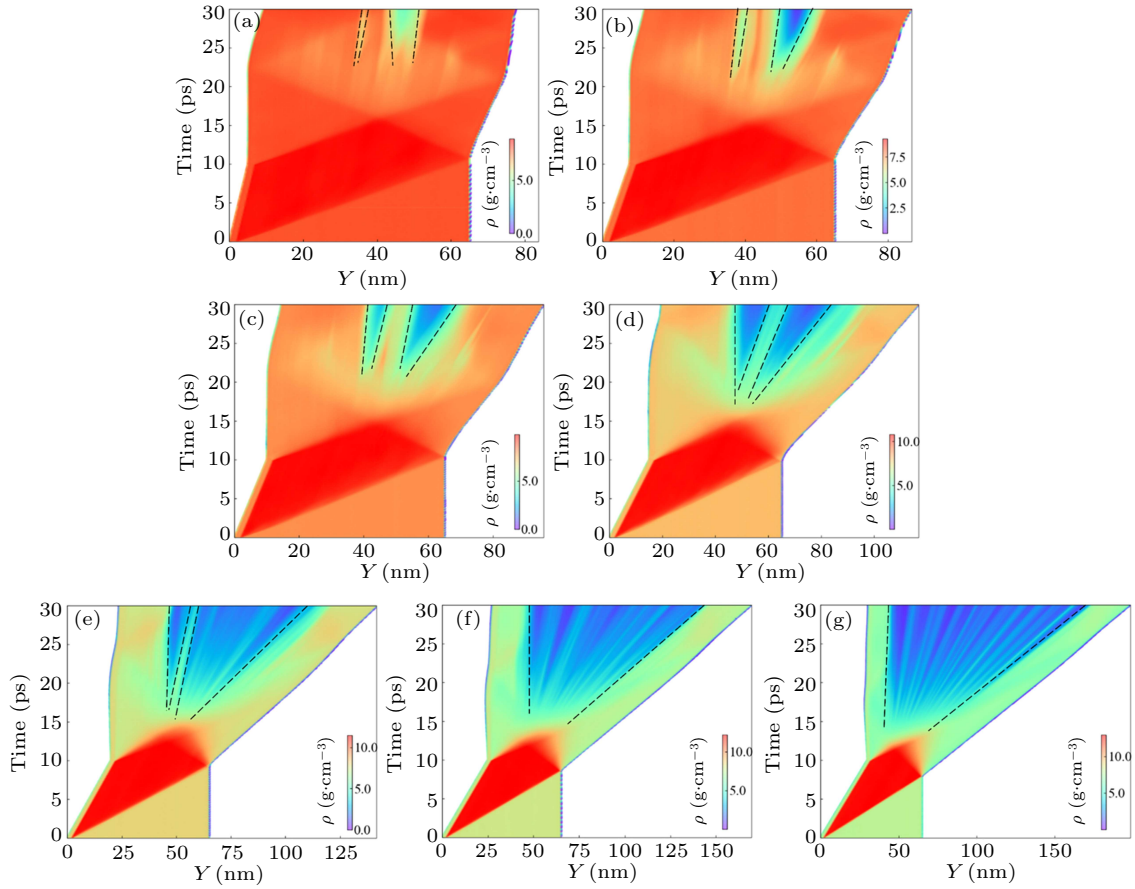


Fig. 9. Position–time diagrams of mass density in the model II: (a) $u_p = 0.5$ km·s^{-1}, (b) $u_p = 0.75$ km·s^{-1}, (c) $u_p = 1$ km·s^{-1}, (d) $u_p = 1.5$ km·s^{-1}, (e) $u_p = 2$ km·s^{-1}, (f) $u_p = 2.5$ km·s^{-1}, (g) $u_p = 3$ km·s^{-1}.

To further elucidate this phenomenon, figure 8 illustrates the evolutionary configurations of voids under different impact velocities (u_p) in model II. The results indicate that, at an impact velocity (u_p) of 1 km·s^{-1}, the model exhibits a limited number of void nucleation points, and spallation evolution is predominantly characterized by the growth and coalescence of a few voids. As the impact velocity (u_p) increases, the number of void nucleation points rises significantly, and the interactions among the voids become more intense, leading to a competitive interaction mechanism. Consequently, at higher impact velocity (u_p), the cavitation behavior of the model proceeds through the aggregation and penetration of some voids while other voids disappear.

As shown in Fig. 9, position–time diagrams of mass density for model II at different impact velocities (u_p) are presented, highlighting the spatial and temporal evolution characteristics of voids in each case. The results demonstrate that the formation of voids leads to a significant decrease in the density of the spall regions (denoted as blue area). With increasing impact velocity (u_p), both the number and volume fraction of microvoids gradually increase, causing the spall regions to evolve from multiple discrete spall planes into a single, larger spall plane. This phenomenon suggests that higher impact velocities (u_p) significantly enlarge the range of spall damage in the model. Notably, the location of the spall damage region remains constant, given that the nucleation points of the voids are uniformly distributed in the central part of the model. Therefore, the increase in impact velocity (u_p) exerts a pronounced influence on both the extent of the spall damage region and the severity of damage.

3.3. Spall strength

To evaluate the spall strength, the critical tensile stress at the onset of the spallation surface was calculated. Figure 10 illustrates the variations in spall strength for the three models at different impact velocities (u_p). The results demonstrate that the variation in spall strength can be classified into four distinct stages with increasing impact velocity (u_p). Notably, an impact velocity of 1.5 km·s^{-1} serves as the critical threshold distinguishing these stages. Stages I and II represent the classical spallation regime, while stages III and IV indicate the micro-spallation regime.

During the classical spallation stage, the spall strength of the model first decreases and then increases, which is consistent with the trends in spall strength variations observed in various alloys through both experimental investigations and numerical simulations.[45,46] During the micro-spallation stage, the spall strength of the model continues to decrease, with a markedly accelerated rate of decline when the impact velocity (u_p) exceeds 2.5 km·s^{-1}.

From the spall strength trends discussed earlier, the three models exhibit consistent variations in their spall strength. Combined with the analysis of damage evolution in the three models, the grain size effect on the models is negligible within this study's scope. As previous research shows a close correlation between microstructural evolution and spall strength changes,[35,41] this paper presents the microstructural evolution of Model II at different impact velocities (u_p), as shown in Fig. 11. It is apparent that the BCC crystal structure of nanocrystalline iron transitions into the face-centered cubic (FCC) structure, HCP structure, and other structural configurations under impact loading conditions. Furthermore, as the impact velocity (u_p) increases, the phase transition time of nanocrystalline iron is significantly reduced, and the phase transition rate is markedly enhanced, indicating a clear four-stage progression.

Stage I: As the impact velocity (u_p) was incrementally increased from 0.5 km·s^{-1} to 1 km·s^{-1}, the phase transition ratio of the crystals remained relatively low and predominantly occurred during the tensile stage. This indicates a transformation from the BCC structure to the FCC structure and other structural configurations under tensile loading conditions. During the relaxation and stretching phases, the other structural configurations gradually reverted to the BCC structure, indicating that the spallation process in nanocrystalline iron is predominantly governed by elastic deformation.

Stage II: The number of phase transitions in the crystals during the compression stage increased significantly as the impact velocity (u_p) was progressively raised from 1 km·s^{-1} to 1.5 km·s^{-1}. Throughout the 1015-ps phase transformation process, the FCC and HCP structures reverted to the BCC structure, whereas the other structural configurations continued to evolve, thereby indicating that the microstructural evolution of nanocrystalline iron is irreversible.

Stage III: As the impact velocity (u_p) was progressively increased from 1.5 km·s^{-1} to 2.5 km·s^{-1}, the rate of transformation from the BCC structure to other structural configurations during the compression stage significantly increased. Concurrently, the proportion of crystal phase transitions from BCC to FCC and HCP during the compression stage gradually decreased, suggesting a substantial increase in the degree of irreversible damage to nanocrystalline iron under impact loading conditions.

Stage IV: At an impact velocity (u_p) of 3 km·s^{-1}, the BCC structure was almost entirely transformed into other structural configurations during the compression phase, with no detectable structural recovery. This suggests that irreversible damage occurred in nanocrystalline iron during the compression phase at this impact velocity (u_p), leading to a significant reduction in its spall strength.

In summary, as the impact velocity (u_p) increased, the damage characteristics of the model transitioned from the tensile stage to the compressive stage and evolved from reversible damage to irreversible damage.

The damage behavior of nanograins under impact loading is generally governed by the intricate thermodynamic response processes that occur within the material. To comprehensively explore the spallation mechanism of nanocrystalline iron at varying impact velocities (u_p), this study compares the thermodynamic evolution paths of model II under diverse impact velocity loading conditions with the melting curves of nanocrystalline iron. However, the modified Ackland potential by Gunkelmann *et al*. exhibits limitations in addressing melting phenomena, potentially leading to insufficient accuracy in the calculated temperature values presented in Fig. 12.[39] Consequently, this study concentrates on analyzing the correlation between specimen temperature variation trends and spall damage evolution, aiming to elucidate the mechanisms underlying the variation of spall strength with impact velocity.

The thermodynamic evolution path is described by the maximum temperature and the corresponding pressure at each time step, while the melting curve of nanocrystalline iron can be described by the following equation:

$$T_m = 1846\left(1+\frac{P}{53.882}\right)^{0.637}. \tag{1}$$

This equation was derived by Zhang *et al*. in their study of nanocrystalline iron melting, where they applied the Ackland potential and fitted the model using Simon's equation.[47] The resulting equation shows improved agreement with the findings of other researchers.[48–50]

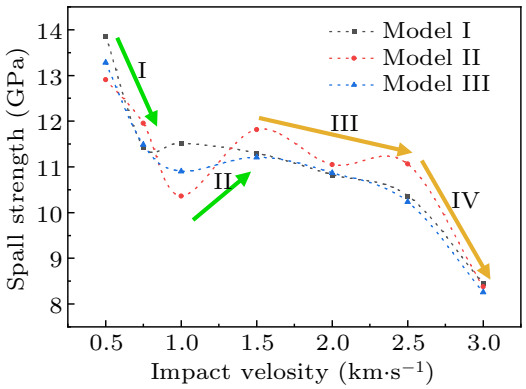


Fig. 10. Variation of spall strength with impact velocity (u_p).

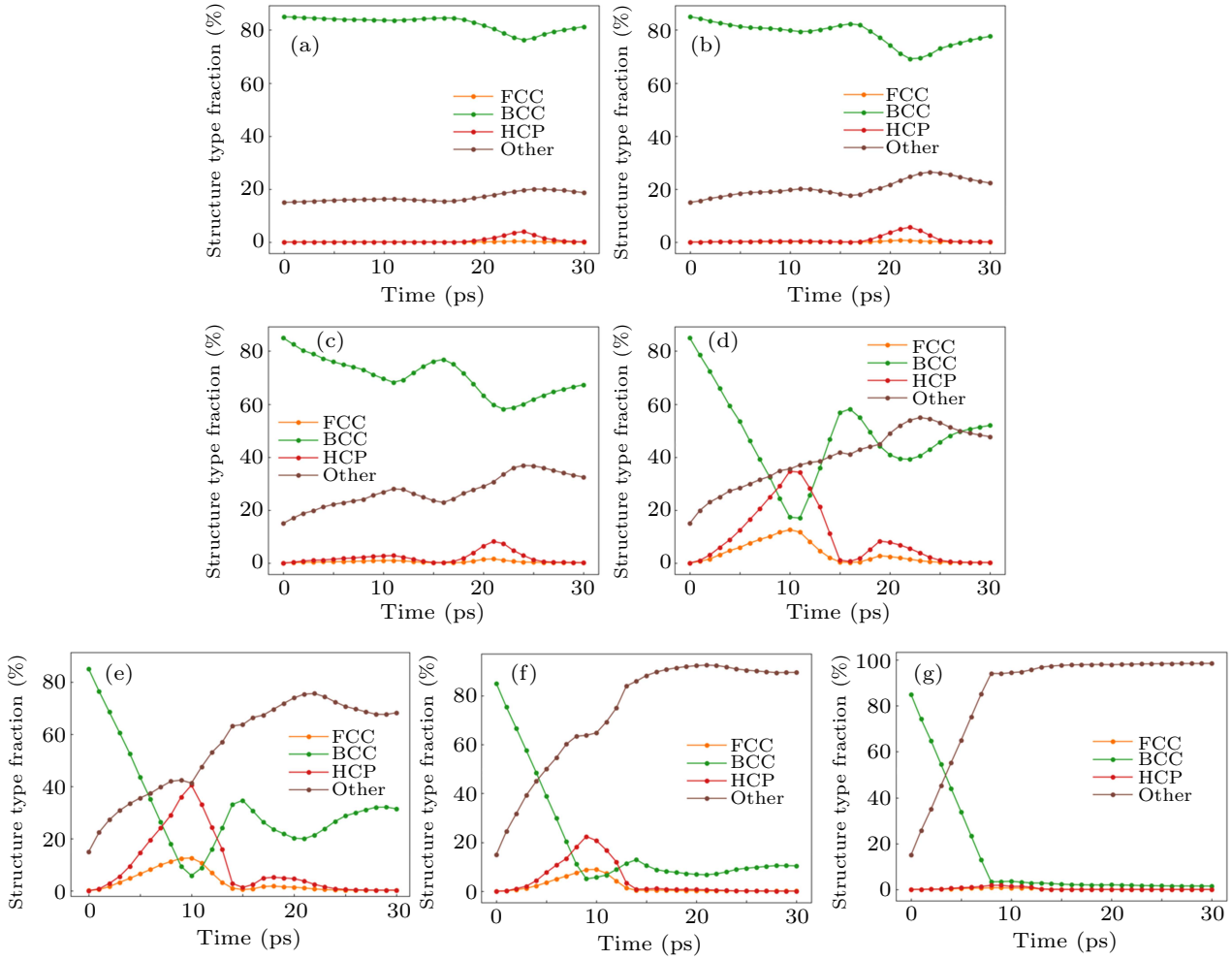


Fig. 11. Shock-induced structural changes of model II: (a) $u_p = 0.5$ km· s^{-1}, (b) $u_p = 0.75$ km·s^{-1}, (c) $u_p = 1$ km·s^{-1}, (d) $u_p = 1.5$ km·s^{-1}, (e) $u_p = 2$ km·s^{-1}, (f) $u_p = 2.5$ km·s^{-1}, (g) $u_p = 3$ km·s^{-1}.

The thermodynamic pathways of nanocrystalline iron at different stages are presented in Fig. 12. It is evident that during stages I and II, the temperature increase in the model predominantly occurs during the stretching phase. In stage I, as the impact velocity (u_p) increases from 0.5 km·s^{-1} to 0.75 km·s^{-1}, the rate of temperature rise during the stretching phase accelerates, and the final temperature becomes significantly higher. This indicates a more pronounced temperature softening effect in nanocrystalline iron, leading to a more rapid reduction in spall strength during this stage. Notably, as the impact velocity (u_p) transitions into stage II, the temperature increase during the stretching phase slows down, and the final temperature deviates further from the model's melting curve. This observation, combined with the structural evolution shown in Fig. 11(b), suggests that a portion of the impact energy contributes to the model's plastic deformation, thereby reducing the energy available for temperature rise. Consequently, the rate of temperature increase gradually diminishes. This is further supported by the observation that the temperature increase at $u_p = 1.5$ km·s^{-1} is lower than that at $u_p = 1$ km·s^{-1}.

In the case of $u_p = 1.5$ km·s^{-1}, although the higher impact velocity generates more energy and raises the model's temperature to a higher level, the melting point of nanocrystalline iron increases due to the strain-rate hardening effect. As a result, the model's temperature did not surpass the melting curve of nanocrystalline iron. Thus, the spallation evolution in stage II is predominantly characterized by plastic deformation, which explains the observed rebound in the spall strength of nanocrystalline iron. When the impact velocity increases from 1.5 km·s^{-1} to 2.0 km·s^{-1}, the model's temperature surpasses the melting curve during the stretching phase. This suggests that the early stage of the spalling process is predominantly governed by plastic damage, while the later stage involves melting-induced damage. This transition is the main factor contributing to the observed reduction in spallation strength. As the impact velocity (u_p) further increases to 2.5 km·s^{-1} and beyond, the model exhibits a temperature rise that surpasses the melting curve during both compression and tension. This demonstrates that the melting-induced damage leads to the complete breakdown of the crystal structure during the compression stage, resulting in a significant reduction in spall strength. Moreover, when the impact velocity (u_p) exceeds 1.5 km·s^{-1}, the temperature rise becomes significantly more dispersed. This is primarily attributed to the expansion of the damage range within the model and the discontinuous variations in temperature and pressure conditions under high-speed impact.

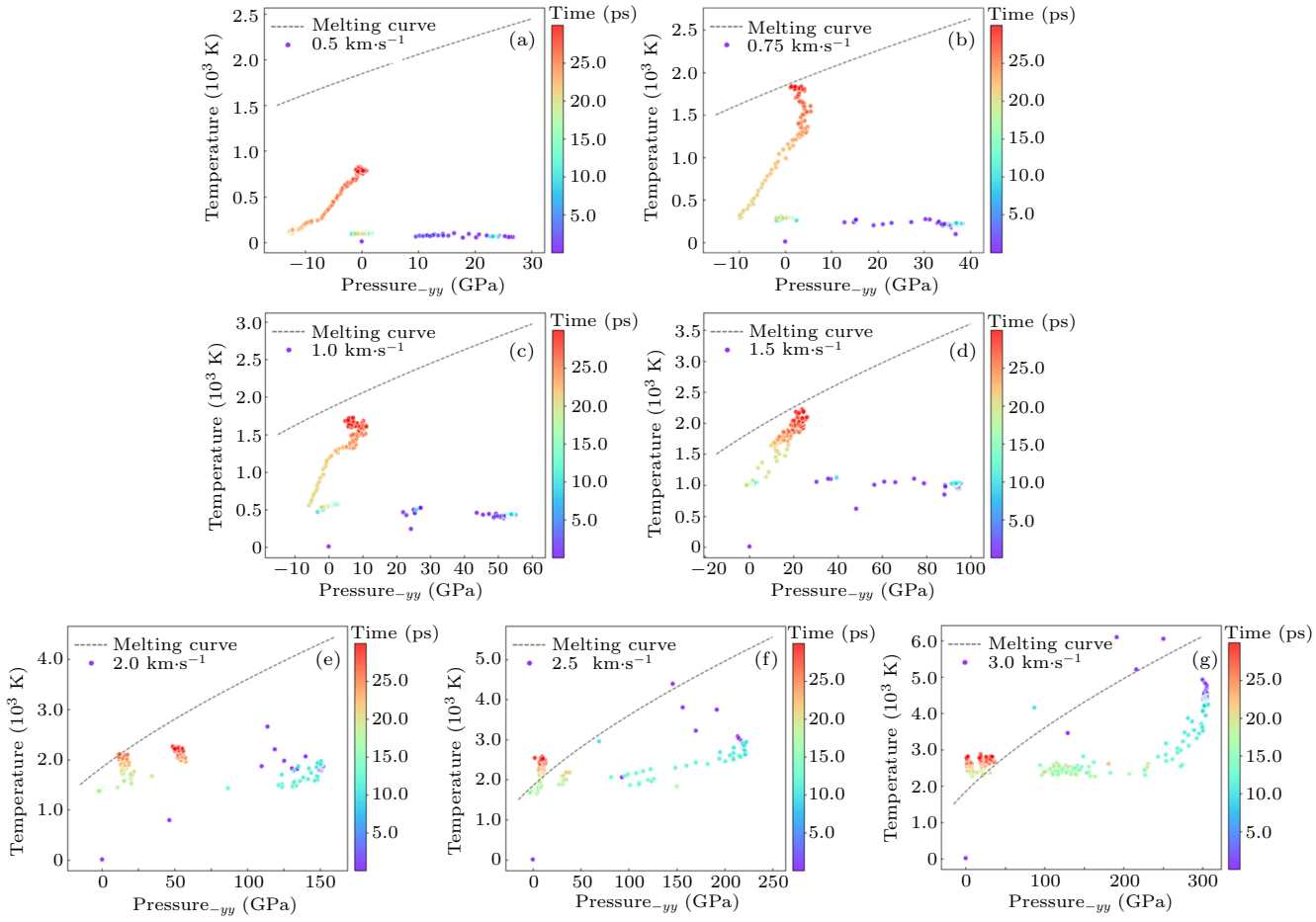


Fig. 12. Local temperature–pressure evolution of model II: (a) $u_p = 0.5$ km· s^{-1}, (b) $u_p = 0.75$ km·s^{-1}, (c) $u_p = 1$ km· s^{-1}, (d) $u_p = 1.5$ km·s^{-1}, (e) $u_p = 2$ km·s^{-1}, (f) $u_p = 2.5$ km·s^{-1}, (g) $u_p = 3$ km· s^{-1}.

3.4. Discussion

This study systematically analyze the mechanisms governing the evolutionary behavior of nanocrystalline iron under impact loading and elucidate the transition of the spall damage mechanism at different impact velocities (u_p), as shown in Fig. 13. In Fig. 13, the vertical axis denotes the evolution time of the model, while the red dashed line marks the cessation of impact compression. The onset of spallation is represented by the black dashed line, corresponding to the initiation of void nucleation. The results indicate that the onset of spallation is significantly accelerated with increasing impact velocity (u_p). Moreover, the horizontal axis represents the variation in impact velocity (u_p). With increasing impact velocity (u_p), melting-induced damage gradually becomes evident during the evolution of the model, leading to a transition in the spallation mechanism from classical spallation to micro-spallation.

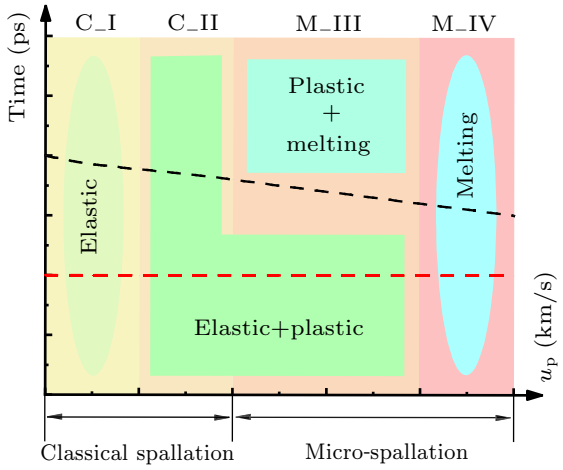


Fig. 13. Spall damage mechanism of nanocrystalline iron at different impact velocities (u_p).

Prior research has established that the spall damage mechanism is dictated by the interaction between strain-rate hardening and thermally-induced softening during the classical spallation process. Within the C_I interval, at relatively low impact velocities (u_p), spall damage is primarily characterized by elastic deformation. During this phase, the thermally-induced softening effect, which is driven by the energy generated from impact loading, predominates over the strain-rate hardening effect. As the impact velocity (u_p) increases, the rate of temperature rise accelerates, leading to a significant reduction in spall strength. Upon further increasing the impact velocity (u_p) and transitioning into the C_II interval, the energy imparted by impact loading is predominantly dissipated through the plastic deformation of nanocrystals. Consequently, this results in a slower rate of temperature rise during the tensile phase of the model. In this stage, the strain hardening effect gradually outweighs the thermally-induced softening effect, thereby promoting a gradual enhancement in spall strength.

The intervals of impact velocity (u_p) associated with micro-spallation in the model are subdivided into two distinct regions. When the impact velocity (u_p) increases and enters the M_III interval, the model undergoes pronounced plastic deformation during the compression phase. During the tensile phase, as the model's temperature approaches the melting point, it demonstrates both plastic deformation and melting behavior. At this stage, the damage mechanism of nanocrystalline iron begins to manifest the features of micro-spallation. The onset of melting is a key factor responsible for the progressive weakening of the model during spallation. Upon reaching the M_IV interval, the local temperature within the model exceeds the melting point during the compression phase. At this stage, the proportion of plastic damage in nanocrystalline iron significantly diminishes, and the damage process is primarily dominated by crystal melting, leading to spall damage. This transition results in an accelerated rate of spallation strength degradation.

4. Conclusions

Based on molecular dynamics simulations, the spall damage patterns in nanocrystalline iron at various impact velocities (u_p) are systematically analyzed. Our results reveal the growth of voids during exfoliation evolution and discuss the effects and mechanisms of impact velocity on spall strength. The main conclusions are summarized as follows:

(i) The mechanisms of spalling in nanocrystalline iron are primarily governed by the impact velocity (u_p), whereas the influence of grain size is relatively minor. As the impact velocity (u_p) increases, the stress distribution within the material transitions from being concentrated at the grain boundaries to becoming more uniform and random. This transition leads to a shift in the fracture mode from cleavage fracture to ductile fracture. When the impact velocity (u_p) exceeds 1.5 km·s^{-1}, the material experiences additional phenomena such as melting, particle ejection, and micro-spallation under impact loading conditions.

(ii) During spallation, the growth rate of the void volume fraction in nanocrystalline iron tends to first increase and then decrease. Furthermore, the timing of hole nucleation advances as the impact velocity increases. At lower impact velocities (u_p), the holes grow progressively and eventually coalesce primarily through a smaller number of holes. At higher impact velocities (u_p), more holes nucleate within the model, resulting in a greater degree of exfoliation damage. Moreover, the increased number of nucleation sites intensifies the competing interactions between the voids, causing some voids to grow larger via growth and aggregation while others vanish.

(iii) As the impact velocity (u_p) increases, the variation in spall strength can be categorized into four distinct stages. In the classical spallation stage, the spall strength of the model

exhibits a decreasing and then increasing trend; in the micro-spallation stage, it shows a decreasing trend, with the rate of decrease significantly increasing when the impact velocity (u_p) exceeds 2.5 km·s^{-1}.

(iv) When classical spallation occurs in nanocrystalline iron, the spall damage is predominantly an elastic–plastic process that gradually transitions from elastic deformation to plastic deformation as the impact velocity (u_p) increases. When micro-spallation occurs in nanocrystalline iron, the spall damage gradually transitions from plastic deformation to melting damage. Additionally, as the impact velocity (u_p) increases, the onset of melting shifts continuously from the tensile phase to the compressive phase.

Acknowledgement

The numerical calculations in this paper have been done on the supercomputing system in the High Performance Computing Center of Southwest Petroleum University.

References

[1] Gianmaria D L, Antonio F, Giusy T and Raffaele L 2021 *Constr. Build. Mater.* **302** 124132
[2] Lian L Y, Zhang X W, Liu Y, Li J and Wang R Q 2023 *Chin. Phys. B* **32** 077501
[3] Sherpa B B, Izumi Y, Inao D, Tanaka S and Hokamoto K 2025 *Mater. Today Commun.* **42** 111536
[4] Kerrouche R, Dadouche A and Boukraa S 2023 *Tribol. Int.* **185** 108495
[5] Wang Y, Liu J, Tang X, Wang Y, An H and Yi H 2023 *Resour. Conserv. Recycl.* **194** 106994
[6] Wei W and Yu X 2020 *Mater. Today Commun.* **24** 101217
[7] Lin F, Wang L, Li Z, Yin L, Wu J, Zheng D, Bao M, Liu P, Zhai H and Shu K 2025 *Int. J. Fatigue* **193** 108760
[8] Mussa A, Krakhmalev P and Bergström J 2020 *Wear* **444–445** 203119
[9] Xie H, Ma T, Yu T and Yin F 2021 *Mater. Today Commun.* **26** 101961
[10] Zhang X, Deng Y, Chen J and Hu W 2021 *Mater. Today Commun.* **29** 102893
[11] Germann T C, Kadau K, Lomdahl P S and Holian B L 2005 *Phys. Rev. B* **72** 064120
[12] Hawreliak J, Colvin J D, Kalantar D H, *et al.* 2006 *Phys. Rev. B* **74** 184107
[13] Kadau K, Germann T C, Lomdahl P S and Holian B L 2002 *Science* **296** 1681
[14] Kadau K, Germann T C, Lomdahl P S and Holian B L 2002 *AIP Conference Proceedings* **620** 351
[15] Peterson E L, Minshall S and Bancroft D 1956 *J. Appl. Phys.* **27** 291
[16] Shockey D, Curran D and Carli P D 1975 *J. Appl. Phys.* **46** 3766
[17] Yaakobi B, Boehly T R, Meyerhofer D D, Collins T J B, Remington B A, Allen P G, Pollaine S M, Lorenzana H E and Eggert J H 2005 *Phys. Rev. Lett.* **95** 075501
[18] Yaakobi B, Boehly T R, Meyerhofer D D, Collins T J B, Remington B A, Allen P G, Pollaine S M, Lorenzana H E and Eggert J H 2005 *Phys. Plasmas* **12** 92703
[19] Wang F M and Ingalls R 1998 *Phys. Rev. B* **57** 5647
[20] Jiang L, Li M, Fu B Q, Cui J C and Hou Q 2024 *Chin. Phys. B* **33** 036103
[21] Kanel' G I, Dremin A N and Anan'in A V 1975 *Combustion, Explosion, and Shock Waves* **9** 381
[22] Johnson P C, Stein B A and Davis R S 1962 *J. Appl. Phys.* **33** 557
[23] Gluzman V D, Kanel' G I, Loskutov V F, Fortov V E and Khorev I E 1985 *Strength Mater-Engl. Tr.* **17** 1093
[24] Gunkelmann N, Bringa E M, Tramontina D R, Ruestes C J, Suggit M J, Higginbotham A, Wark J S and Urbassek H M 2014 *Phys. Rev. B* **89** 140102
[25] Gunkelmann N, Tramontina D R, Bringa E M and Urbassek H M 2014 *New J. Phys.* **16** 093032
[26] Wang K, Zhu W, Xiao S, Chen K, Deng H and Hu W 2015 *Int. J. Plast.* **71** 218
[27] Wang K, Xiao S, Deng H, Zhu W and Hu W 2014 *Int. J. Plast.* **59** 180
[28] Amadou N, Rességuier T D, Dragon A and Brambrink E 2018 *Phys. Rev. B* **98** 024104
[29] Yu J, Shao J, Shu H, Huang X and Fu S 2024 *Mater. Today Commun.* **39** 109291
[30] Jiang S, Huang Y, Wang K, Li X, Deng H, Xiao S, Zhu W and Hu W 2021 *J. Appl. Phys.* **130** 015107
[31] Huang Y, Xiong Y, Li P, Li X, Xiao S, Deng H, Zhu W and Hu W 2019 *Int. J. Plast.* **114** 215
[32] Zhang X, Chen J, Hu W, Zhu W, Xiao S, Deng H and Cai M 2019 *J. Appl. Phys.* **126** 045901
[33] Zhang X, Wang K, Zhu W, Chen J, Cai M, Xiao S, Deng H and Hu W 2018 *J. Appl. Phys.* **123** 045105
[34] Wu L, Wang K, Xiao S, Deng H, Zhu W and Hu W 2016 *Comput. Mater. Sci.* **122** 1
[35] Zhang F,Dong J Q, Xie Z Y, He Z Y, Shu H, Wang R R, Xiong J, Jia G, Fang Z H, Wang W, Xiao D W, Lei A L, Chen J and Huang X G 2024 *Chin. Phys. B* **33** 106101
[36] Cui X, Zhu W, He H, Deng X and Li Y 2008 *Phys. Rev. B* **78** 024115
[37] Thompson A P, Aktulga H M, Berger R, Bolintineanu D S, Brown W M, Crozier P S, in 't Veld P J, Kohlmeyer A, Moore S G, Nguyen T D, Shan R, Stevens M J, Tranchida J, Trott C and Plimpton S J 2022 *Comput. Phys. Commun.* **271** 108171
[38] Amadou N and Rességuier T D 2023 *Phys. Rev. B* **108** 174109
[39] Urbassek H M, Ackland G J, Bringa E M, Gunkelmann N, Ruestes C J and Kang K 2012 *Phys. Rev. B* **86** 144111
[40] Hoang-Thien Luu R J R, Martin Rudolph, Eduardo M Bringa, Timothy C Germann, David Rafaja, and Gunkelmann N 2020 *Phys. Rev. B* **102** 020102
[41] Feng L, Zhang X, Li W, Xiang M and Yao X 2023 *Int. J. Mech. Sci.* **256** 108536
[42] Stukowski A 2010 *Model. Simul. Mater. Sci. Eng.* **18** 015012
[43] Wu D, Zhu Y, Zhao L, Huang M and Li Z 2021 *J. Appl. Phys.* **129** 175110
[44] Chen P, Wang X, Wang P and He A M 2022 *Int. J. Mech. Sci.* **220** 107122
[45] Zhu Y, Hu J, Wei Q, Zhang J, Sun Y, Luo G and Shen Q 2023 *Mech. Mater.* **186** 104809
[46] Ma K and Dongare A M 2022 *J. Mater. Sci.* **57** 12556
[47] Zhang W, Liu Z, Liu Z and Cai L 2015 *Phys. Earth Planet. Inter.* **244** 69
[48] Alf D, egrave, Price G D and Gillan M J 2002 *Phys. Rev. B* **65** 165118
[49] Bouchet J, Mazevet S, Morard G, Guyot F and Musella R 2013 *Phys. Rev. B* **87** 094102
[50] Luo S N, Strachan A and Swift D C 2004 *J. Chem. Phys.* **120** 11640